PAPER

Vertical SnO$_2$ nanosheet@SiC nanofibers with hierarchical architecture for high-performance gas sensors†

Bing Wang,[a] Yingde Wang,*[a] Yongpeng Lei,*[b] Song Xie,[a] Nan Wu,[a] Yanzi Gou,[a] Cheng Han,[a] Qi Shi[a] and Dong Fang[c]

Increasing demands for detection of harmful gases in harsh environments have stimulated considerable efforts to develop a novel gas sensor with high sensitivity, superior thermal/chemical stability and fast response/recovery rate. In this paper, we report the vertical growth of ultrathin SnO$_2$ nanosheets (SnO$_2$ NSs) on quasi-one-dimensional SiC nanofibers (SiC NFs) forming a hierarchical architecture *via* a simple hydrothermal method. In comparison to pure SnO$_2$ NSs, the SnO$_2$ NS@SiC NF hierarchical composite shows an ultrafast response/recovery rate, high sensitivity, and simultaneously excellent reproducibility to various target gases including ethanol, methanol, hydrogen, isopropanol, acetone and xylene, even at high temperature. The response times are less than 5 s with corresponding recovery times <15 s. Furthermore, the SnO$_2$ NS@SiC NF gas sensor shows a superior sensing selectivity and long-term stability to ethanol. The hierarchical architecture and synergetic effect of the SnO$_2$–SiC heterojunction as well as plenty of active sites from the vertically ultrathin SnO$_2$ NSs have critical effect on the superior sensing performance of SnO$_2$ NS@SiC NFs. This work highlights the possibility to develop a novel high-performance gas sensor for application in harsh environments.

Introduction

In situ detection of gases hazardous to the environment and human health has attracted increasing attention.[1,2] In the past few decades, metal-oxide semiconductor based gas sensors have been extensively investigated for various daily and industrial applications due to their outstanding sensing performance, even in harsh environments.[1,3,4] Thereto, n-type tin dioxide (SnO$_2$) has been proved to be promising for gas sensing by virtue of its excellent photoelectrical properties, superior thermal stability (melt point is 1127 °C), chemical inertness, low cost and non-toxicity.[5,6] The sensing mechanism of SnO$_2$ gas sensors is based on the electrical conductivity change of the sensor in different types of target gases.[7] In general, when SnO$_2$ is exposed to air, the electron from its conduction band (CB) will transfer to the absorbed oxygen, resulting in the production of tremendous oxygen species (O^{2-}, O$^-$ or O$_2^-$) on the SnO$_2$ surface. Simultaneously, an electron-depleted surface layer forms on SnO$_2$, which leads to a decrease in the electrical conductivity. In reducing gases (*e.g.*, ethanol, hydrogen, and methanol), the target gases will react with those oxygen species, freeing electrons back to the SnO$_2$ surface, leading to an increase in the sensor conductivity.[8] In oxidizing gases (electron acceptor), more electrons are grabbed by the absorbed gases, further lowering the electrical conductivity of the sensor. Recently, SnO$_2$ with different nanostructures (nanosheets, nanoparticles, nanowires, nanospheres, nanotubes, *etc.*) has been reported for detecting various types of gases.[8] Moreover, to reach higher sensitivity, strategies such as doping with noble metals,[9,10] forming heterojunctions with other semiconductors[11,12] and exposing active facets[13] have been demonstrated.

Besides sensitivity and durability, the response/recovery behavior is also a vital characteristic parameter for gas sensors. With a fast response/recovery rate, large loss/harm can be averted in time. However, achieving rapid response and recovery characteristics for these nanostructured gas sensors is still a challenge.[14] To promote the response/recovery speed, a promising way is to construct hierarchical architectures, which can simultaneously avoid the agglomeration of SnO$_2$ nanostructures and facilitate the diffusion (adsorption and desorption) of target gas.[15] For instance, Lee *et al.* have demonstrated that the core–shell ZnO–SnO$_2$@carbon

[a] *Science and Technology on Advanced Ceramic Fibres and Composites Laboratory, National University of Defense Technology, 109 Deya Road, Changsha 410073, P. R. China. E-mail: wyd502@163.com*

[b] *College of Basic Education, National University of Defense Technology, Changsha 410073, P. R. China. E-mail: lypkd@163.com*

[c] *College of Materials Science and Engineering, Wuhan Textile University, Wuhan 430074, P. R. China*

† Electronic supplementary information (ESI) available: Figures and tables. See DOI: 10.1039/c5tc02792f

This journal is © The Royal Society of Chemistry 2016

J. Mater. Chem. C, 2016, **4**, 295–304 | 295

nanofibers exhibited excellent sensing performance including fast response/recovery properties, high sensitivity and ultralow detection limit.[16] The polypyrrole/SnO_2 hybrid also showed very fast response and high sensitivity to ammonia gas.[17] Three-dimensional mesoporous graphene aerogel has been utilized to support SnO_2 nanocrystals for a high performance NO_2 gas sensor.[18] However, most of the reported substrates including carbonaceous materials (graphene, carbon nanotubes, carbon nanofibers, *etc.*) and organic substrates (poly(ethylene terephthalate), polypyrrole and polyimide) cannot meet the requirements to apply in certain fields like ethanol direct solid oxide fuel cells (EDSOFCs), power generation, aerospace, automotive, avionics, industrial process control, nuclear power and well-logging industries due to the harsh work environments (*e.g.*, high temperatures, corrosive environments, and high frequency).[19–23] For instance, ethanol gas sensors have been widely applied in breath analyzers for drivers, detecting ethanol in foodstuff experiments to assess the development of bacteria and fungi in food and monitoring the chemical processes in chemical industries.[24] However, most of the reported studies were focused on the low/room temperature ethanol gas sensors because they are more desired for application in the fields mentioned above. But these ethanol sensors cannot satisfy the requirements to monitor the ethanol leakage and/or its total combustion process in the EDSOFCs, whose operating temperature is typically in the range of 500–1000 °C.[22,23] Hence, it is more desired but challenging to develop a novel gas sensor capable of withstanding aforementioned harsh environments.

As a wide band gap semiconductor, silicon carbide (SiC) has emerged as an ideal candidate for application in harsh environments.[25] More recently, SiC based gas sensors have attracted increasing attention due to their chemical inertness, excellent thermal stability, high thermal conductivity, high electron mobility, and compatibility with conventional Si-based integrated devices.[26,27] The high electron mobility of SiC is beneficial to quickly shuttle the charge carriers, which offers an opportunity to design the SiC based gas sensor with an ultrafast response/recovery rate. Therefore, combining SiC with highly reactive SnO_2 is expected to develop a novel high performance gas sensor capable of applying in harsh environments. Furthermore, it has been demonstrated that the composite of SnO_2 nanobelt@SiC foams showed efficient performance to detect low concentration of NH_3 and NO_2,[28] whereas the response/recovery speed was very slow.

In the present paper, ultrathin SnO_2 nanosheets (SnO_2 NSs) were *in situ* grown on the quasi-one-dimensional SiC nanofibers (SiC NFs) forming a hierarchical SnO_2 NS@SiC NF composite *via* a simple hydrothermal method. The synthesized SnO_2 NS@SiC NF sample shows a high sensitivity, excellent reproducibility, outstanding selectivity, long-term stability and particularly ultrafast response/recovery speed toward ethanol. Such a superior sensing performance is attributed to the synergetic effect of SnO_2 and SiC and the hierarchical architectures as well as plenty of active sites from the vertically ultrathin nanosheets with large surface to volume ratios. This work demonstrates a simple strategy to design a high performance gas sensor which can be applied in harsh environments.

Experimental section

Materials

Polyacrylonitrile (PAN, M_n = 120 000 g mol^{-1}, Kaneka, Japan), Si powders (200 mesh, Sinopharm, China), tin dichloride dihydrate ($SnCl_2 \cdot 2H_2O$, Sigma-Aldrich Co., UK), mercaptoacetic acid (MA, Sigma-Aldrich Co., UK), *N,N*-dimethylformamide (DMF, Hengxing, China), NaOH (Sigma-Aldrich Co., UK) and HCl (37 wt%, Hengxing, China) were of all analytical reagents and used as-received without any further purification.

Fabrication of mesoporous SiC NFs

Typically, 1.2 g of PAN powders were dissolved in 10 ml of DMF under vigorous stirring at 30 °C for 5 h to prepare the spinning solution. And then the homogeneous spinning solution was loaded into a 10 ml volume plastic syringe with a needle of 0.8 mm inner diameter. Electrospinning was carried out with a power supply (Dongwen, China) of 18 kV applied on the needle and the aluminum foil film collector with a distance of 25 cm. The feed rate was kept at 0.9 ml h^{-1} using a syringe pump (Longer Pump LSP02-1B, China). After curing the as-received PAN nanofibers at 260 °C for 1 h in flowing air (1 °C min^{-1}), the obtained nanofibers were carbonized at 1000 °C for 1 h (2 °C min^{-1}) to obtain CNFs. To synthesize SiC NFs, excessive Si powders were placed at the bottom of the alumina crucible and the as-received CNFs were laid on the top of the silicon powders with a distance of 1.5 cm. Then the alumina crucible was heated to 1500 °C for 5 h (10 °C min^{-1}) in a horizontal furnace (Tianjin Zhonghuan, China) under an Ar atmosphere.

Alkali treatment of the SiC NFs

Prior to hydrothermal reaction, the resultant SiC NFs were treated with alkali solution. In detail, 25 mg of SiC NFs were immersed in 20 ml of NaOH solution (5 M) for 12 h at room temperature. Afterward, the treated SiC NFs were washed with deionized water 5 times and dried at 80 °C for 12 h.

Fabrication of the hierarchical SnO_2 NS@SiC NFs

SnO_2 NSs were *in situ* grown on the alkali-treated SiC NFs by a simple hydrothermal method. Typically, 0.1 g $SnCl_2 \cdot 2H_2O$ was dissolved in 30 ml MA solution (10 mM), followed by adding 0.5 g urea and 0.5 ml HCl solution. The mixture solution was stirred for 2 min in air at 25 °C and then was transferred into the Teflon-lined stainless-steel autoclave. Subsequently, 10 mg of the basic-treated SiC NFs were immersed into the above solution. The autoclave was sealed up and heated to the target temperature (100–180 °C) in an electric oven and maintained for 6 h. After naturally cooling to the room temperature, the resultant sample was washed with a mixture solvent of ethanol and water (v/v = 1 : 1) several times and dried at 80 °C for 12 h. Finally, the samples were calcined at 600 °C for 2 h with a heating rate of 5 °C min^{-1}.

Characterization

The morphological features of the catalysts were analyzed by using a Hitachi S-4800 field-emission scanning electron

296 | *J. Mater. Chem. C*, 2016, **4**, 295–304

This journal is © The Royal Society of Chemistry 2016

microscope (FE-SEM) with an acceleration voltage of 5.0 kV and a JEM-2100 high resolution transmission electron microscope (HRTEM). X-ray diffraction (XRD) data were collected from 10 to 80° (2θ) on a Bruker AXS D8 Advance device using Cu-Kα radiation (λ = 1.5418 Å) at a scanning rate of 2θ = 0.02° per step. X-ray photoelectron spectroscopy (XPS) was conducted on a Thermo Scientific ESCALAB 250Xi machine with an Al Kα source. And the spectra were quantified and analyzed using XPSPEAK 4.1 software. The thermal stability of the SnO$_2$ NSs@SiC NFs was evaluated at the temperature range from 30 to 800 °C by using a thermogravimetric analyzer (Pyris 1 TGA, PerkinElmer) with a heating rate of 10 °C min^{-1} in air. The Brunauer–Emmett–Teller (BET) surface areas (S_{BET}) of samples were estimated from the nitrogen adsorption isotherm (BELSORP-mini II, Japan). The pore size distributions were determined using the Barrett–Joyner–Halenda (BJH) method.

Gas sensing measurements

The gas sensing performances of the samples were measured in an intelligent gas sensor analysis system (CGS-1TP, Beijing Elite Tech Co., Ltd., China) as shown in Fig. 1a, which was commonly used to test the gas sensing behaviors.[18] The operating temperature can be modulated from room temperature to 500 °C with a heating rate of 5 °C s^{-1}. First, the prepared sensing materials were mixed with deionized water (10 mg ml^{-1}) to form a homogeneous paste. Gas sensing devices were fabricated by coating the pastes (20 μl) on commercial aluminium substrates (10 mm × 5 mm × 0.25 mm) with Au interdigitated electrodes (AURORA technologies, China) as illustrated in Fig. 1b. Subsequently, the prepared sensors were naturally dried in air for several hours. During the sensing measurement, the Au electrodes were pressed under the metal probes to achieve electrical contact (Fig. 1a). After the sensor was heated to the target temperature and the resistance kept at almost a constant level, the calculated amount of target gases (chromatographic pure) was injected into the test chamber (18 L in volume). At the same time, the fans were turned onto ensure a uniform concentration of the target gases in the chamber. Finally, the test chamber was opened to make the sensor exposing to air that the resistance of the sensor was recovered. The sensor response (sensitivity) is defined as $S = R_g/R_a$ in reducing gases for the n-type semiconductor, where R_a and R_g are the resistance of the sensor in air and in the target gas, respectively. The response/recovery time was defined as the time needed to reach 90% of the saturation resistance change after introducing target gas or exposing in air.

Results and discussion

The SnO$_2$ NS@SiC NF hybrids were synthesized by growing vertical SnO$_2$ NSs on the SiC NFs via a simple hydrothermal method as illustrated in Scheme 1. Prior to hydrothermal reaction, the as-received SiC NFs were treated in 5 M NaOH solution to introduce hydroxyl (–OH) groups as well as to remove the silica on the surface of SiC NFs. After immersing SiC NFs into the mixed solution of SnCl$_2$, urea and MA, Sn^{2+} with positive charge was easily absorbed onto the OH-terminated SiC NFs (negative charge) due to the electrostatic interactions. During the hydrothermal reaction, tin oxides (SnO$_x$) firstly nucleated on the SiC NFs followed by the Ostwald ripening process to form the nanosheet morphology. Urea in the solution can promote the nucleation of Sn^{2+} to form nanocrystals while MA plays a critical role in the formation of nanosheets.[18,29] Moreover, the higher hydrothermal reaction temperature leads to the fast nucleation and growth of SnO$_2$ crystals, thus forming rod-shaped SnO$_x$ on the SiC NFs. In addition, the abundance of –OH groups and MA additives cannot only ensure the formation of NSs, but also enable the SnO$_2$ NSs to connect with SiC NFs tightly, which will minimize the boundary and promote the electron transfer between the SnO$_2$ NSs and SiC NFs. The zeta potential of SnO$_2$ NS@SiC NFs is measured to be −11.1 mV, implying that the SnO$_2$ NS@SiC NFs are highly negatively charged (Fig. S1, ESI†).

Fig. 2 shows the XRD pattern and TGA analysis of the resultant SnO$_2$ NS@SiC NF hierarchical composite. It is clear that the hierarchical composite is composed of two mixed phases of tetragonal rutile SnO$_2$ (JCPDS card no. 41-1445) and cubic SiC (JCPDS card no. 29-1129) (Fig. 2a).[27,30] The sharp peaks and the absence of other impurities imply a high crystallinity and purity of the hierarchical composite. The average crystallite size of the SnO$_2$ NSs is calculated to be 10 nm by using the Scherrer formula: $d = 0.9\lambda/B\cos\theta$, where B is the width of the diffraction peak at half its maximum intensity, λ is the X-ray wavelength, and θ is the maximum diffraction angle. To investigate the stability of the SnO$_2$ NS@SiC NF sample, the TGA test was conducted from room temperature to 800 °C in air. As shown in Fig. 2b, the weight loss occurred below 100 °C is ascribed to the evaporation of water and other absorbed
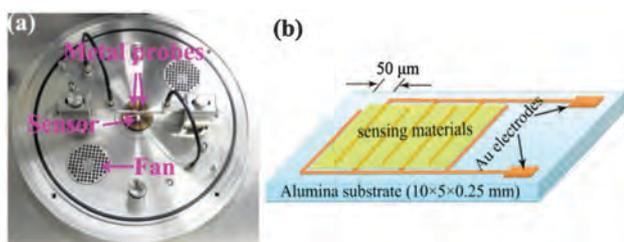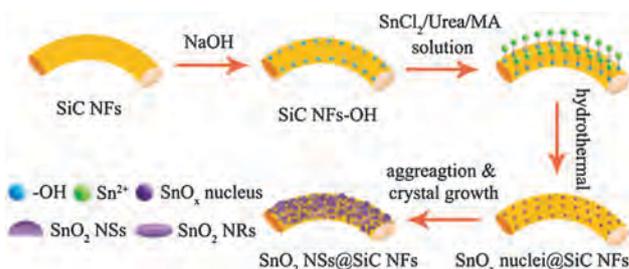

Fig. 1 (a) Photograph of the gas sensing testing equipment CGS-1TP and (b) schematic illustration of the gas sensor device.

Scheme 1 Schematic illustration of the synthesis process for SnO$_2$ NS@SiC NFs.
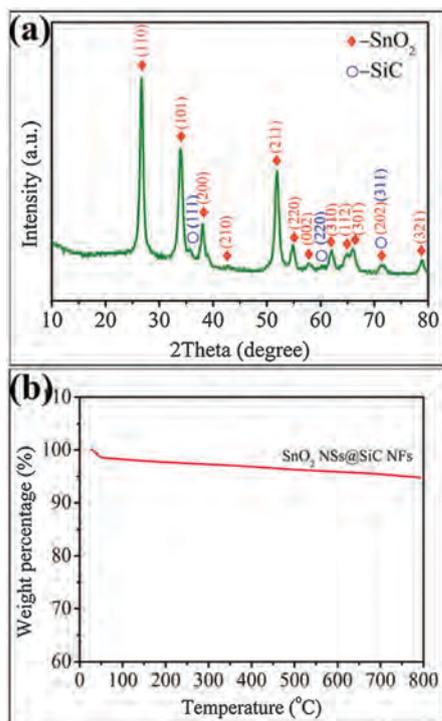
Fig. 2 (a) XRD pattern and (b) TGA analysis of the SnO$_2$ NS@SiC NF hierarchical composite.

species. There is no dramatical weight change along with the increasing temperature to 800 °C, suggesting the excellent stability and great potential of the sample for high temperature application.

The morphologies and microstructures of the SiC NFs and SnO$_2$ NS@SiC NF hybrids were characterized by SEM (Fig. 3).

For SiC NFs, a rough fiber surface is observed (Fig. 3a), which is beneficial for the nucleation of SnO$_x$. According to the general SEM image (Fig. 3b), SnO$_2$ NSs are uniformly grown on all of the SiC NFs without existing in the gap of the fibers at the reaction temperature of 120 °C. The diameter of the SnO$_2$ NS@SiC NF hybrid is about 400 nm in comparison to 200 nm of the pure SiC NFs, implying that the vertical SnO$_2$ NS is about 100 nm in height. As shown in Fig. 3c, it is obvious that the well-defined ultrathin SnO$_2$ NSs are interconnected with each other, supplying a multipath electron transfer channel, which may be propitious to accelerate the response rate. The thicknesses of the interconnected SnO$_2$ NSs are calculated to be less than 5 nm (inset in Fig. 3c). At a low reaction temperature of 100 °C, no SnO$_2$ NSs but nanoparticles are generated on the SiC NFs (Fig. S2a, ESI†), while SnO$_2$ nanorods (SnO$_2$ NRs) are observed on the SiC NFs when the temperature rises up to 160 °C (Fig. S2b, ESI†). From the viewpoint of architecture, more SnO$_2$ located on the surface of ultrathin SnO$_2$ NSs can react with the target gas due to the high surface to volume ratio of nanosheets. In the case of SnO$_2$ NRs, SnO$_2$ in the internal of the nanorods cannot contact with the target gas, leading to the relatively low availability of the SnO$_2$ NSs. It is also demonstrated that there are four elements Si, C, O and Sn in the SnO$_2$ NS@SiC NF composite from the EDS spectrum (Fig. 3d). The Au element is from the sputtered Au particles for SEM measurement.

Fig. 4 shows the TEM images of SiC NFs and SnO$_2$ NS@SiC NF hierarchical composites. SiC NFs with a diameter of about 200 nm and rough surfaces are clearly illustrated in Fig. 4a. The HRTEM image in Fig. 4b reveals the lattice spacing of 0.251 nm
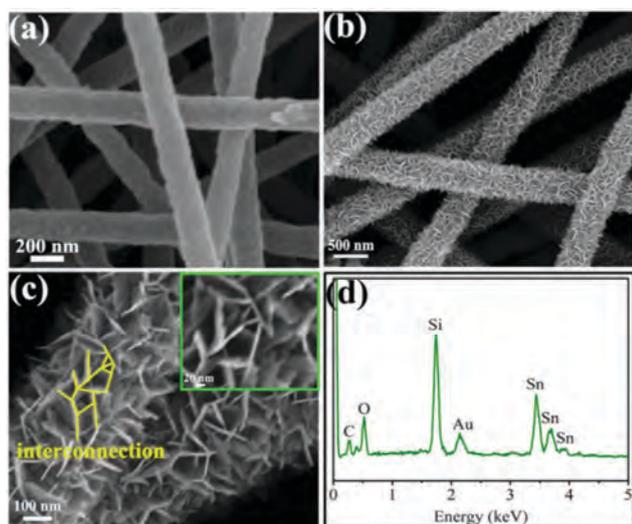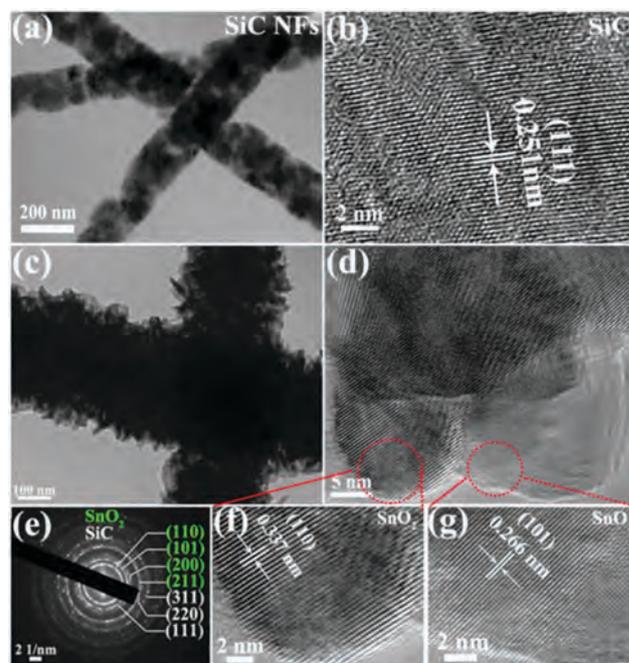

Fig. 3 SEM images of (a) SiC NFs and (b) the SnO$_2$ NS@SiC NF hierarchical hybrids synthesized at the reaction temperatures of 120 °C at low magnification; (c) at high magnification; (d) EDS spectrum of the SnO$_2$ NS@SiC NF hybrid. The inset in (c) is the close view of the interconnected NSs with the thickness less than 5 nm.

Fig. 4 (a) TEM images of (a) SiC NFs and (c) SnO$_2$ NS@SiC NFs at low magnification; (b) and (d) the corresponding HRTEM images of SiC NFs and SnO$_2$ NS@SiC NFs, respectively; (e) SAED of SnO$_2$ NS@SiC NFs; (f) and (g) magnified HRTEM image of the SnO$_2$ NSs.

298 | J. Mater. Chem. C, 2016, 4, 295–304

This journal is © The Royal Society of Chemistry 2016

assigned to the (111) plane of SiC. For SnO₂ NS@SiC NFs, the overall TEM image (Fig. 4c) indicates that SiC NFs are uniformly covered by SnO₂ NSs with the thickness of several nanometers. The composite fiber is of 400 nm in diameter, which is in agreement with the SEM result (Fig. 3b). The selected area electron diffraction (SAED, Fig. 4e) pattern of the SnO₂ NS@SiC NF hybrids with well-defined rings is composed of two parts. The rings from inside to outside with the corresponding planes marked with blue colour are indexed to (110), (101), (200) and (211) planes of rutile SnO₂, while the rings from inside to outside with the corresponding planes marked with white colour are indexed to (111), (220) and (311) planes of cubic SiC. As shown in the HRTEM image (Fig. 4d), the fan-shaped SnO₂ NSs with tens of nanometers in width are clearly observed. The fringe spacing of 0.337 and 0.266 nm (Fig. 4f and g) have also been demonstrated, which are consistent with the (110) and (101) planes of SnO₂ NSs.[12,31] These results further confirm the hierarchical structure of SnO₂ NS@SiC NFs, which is composed of rutile SnO₂ and cubic SiC as depicted in the XRD pattern (Fig. 2a). To further investigate the chemical composition and bonding states, XPS analysis of the SnO₂ NS@SiC NF hybrid is carried out. Fig. 5a exhibits the survey scan XPS spectrum of the SnO₂ NS@SiC NFs, which confirms the presence of four elements including Si, C, Sn and O in the sample. The high resolution Sn 3d spectrum (Fig. 5b) shows two typical peaks at the binding energies of 495.1 and 486.7 eV corresponding to the Sn $3d_{3/2}$ and Sn $3d_{5/2}$ states of Sn^{4+} with spin–orbit splitting of 8.4 eV, indicating the presence of SnO₂.[18,32,33] The deconvolution of the O 1s peak (Fig. 5c) displays four peaks at 530.4, 531.0, 532.0 and 532.9 eV, which belong to the O^{2-} and/or O–Sn bond in SnO₂, O^-, O_2^- and –OH, respectively.[4,34] These oxygen species (O^{2-}, O^- and O_2^-) may originate from the adsorption of oxygen on the surface of SnO₂ followed by receiving electrons from the CB of SnO₂. As known, large amounts of oxygen species are beneficial for enhancing
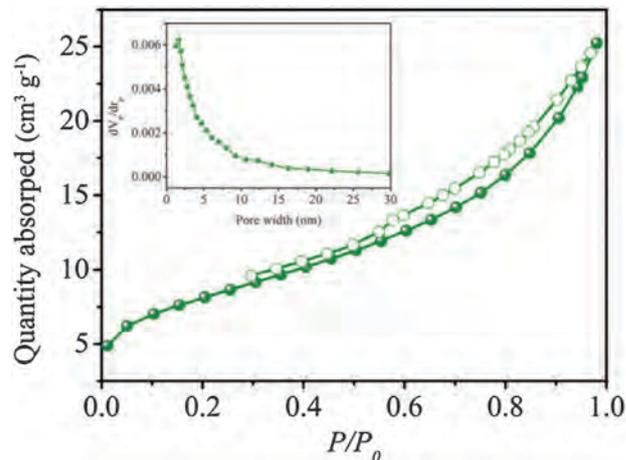

Fig. 6 N₂ adsorption–desorption isotherm of SnO₂ NS@SiC NFs. The inset is the corresponding pore size distribution.

the sensitivities of gas sensors. The deconvoluted O 1s peaks at higher binding energy may be ascribed to the chemisorbed-OH (from H₂O) on the surface of SnO₂.[35] In the Si 2p high resolution spectrum (Fig. 5d), the peak at the binding energy of 101.0 eV representing the Si–C bond is observed, implying the existence of SiC. Additional peaks at 102.1 and 103.4 eV in Fig. 5d are ascribed to the Si–O(H) and Si–O₂ bonds in the SiC NFs,[36] which may be attributed to the surface oxidization of SiC during hydrothermal reaction and/or the attached –OH group on SiC after basic treatment.

The specific surface area and pore size distribution of the SnO₂ NS@SiC NF hierarchical composite were further characterized by N₂ adsorption–desorption measurements. The isotherm illustrated in Fig. 6 reveals a typical IV adsorption branches with a H3 hysteresis loop according to IUPAC classification,[37] implying that there are abundant slit-shaped mesopores resulted from the packed nanosheet-like SnO₂ on the SiC NFs. The BET surface area of SnO₂ NS@SiC NFs is calculated to be 28.6 m² g⁻¹ with a total pore volume of 0.04 cm³ g⁻¹. The pore size distribution determined by the BJH method is calculated to be in the range of 0.2–15 nm. While the BET surface area of pure SnO₂ NSs is 14.1 m² g⁻¹ with a total pore volume of 0.016 cm³ g⁻¹ (Fig. S3, ESI†). The results indicate that the hierarchical SnO₂ NS@SiC NFs have a higher sensing area than the pure SnO₂ NSs. The low surface area may be attributed to the aggregation of the pure SnO₂ NSs as shown in the SEM image (Fig. S4, ESI†).

The gas sensing performances of the commercial SnO₂ powders, pure SnO₂ NSs and SnO₂ NS@SiC NF hierarchical composites were evaluated by their resistance changes upon exposure to target gases with a controlled concentration. It is well known that the response of the gas sensor is greatly affected by the operating temperature. To determine the optimum one, all of the gas sensors were tested at the temperature from 200 to 500 °C towards 100 ppm ethanol as the results exhibited in Fig. 7a. It can be seen that the sensitivities of pure SnO₂ NS and SnO₂ NS@SiC NF sensors are higher than that of commercial
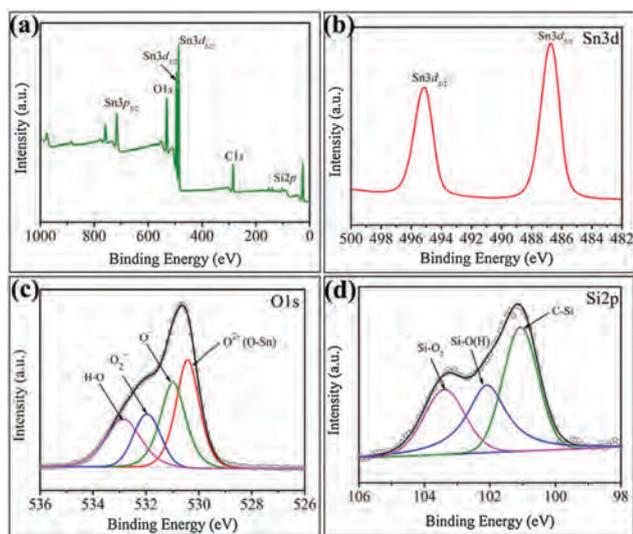

Fig. 5 XPS analysis of SnO₂ NS@SiC NFs: (a) survey spectrum; (b) Sn 3d; (c) O 1s and (d) Si 2p.
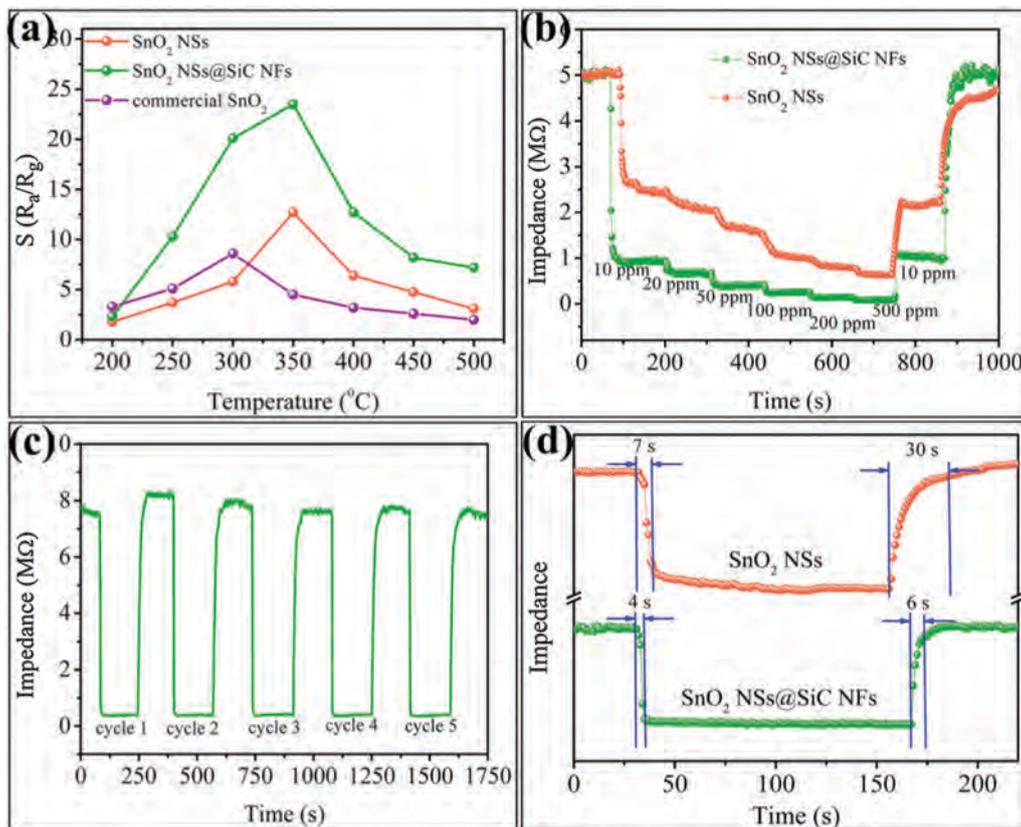
Fig. 7 (a) Sensor responses of the pure SnO_2 NSs and SnO_2 NS@SiC NFs to 100 ppm ethanol at different operating temperatures; (b) dynamic sensing response of pure SnO_2 NSs and SnO_2 NS@SiC NFs toward various ethanol concentrations at 350 °C; (c) sensing reproducibility of the SnO_2 NS@SiC NF hierarchical composite sensor and (d) comparison of the response time and recovery time between pure SnO_2 NSs and SnO_2 NS@SiC NFs; ethanol concentration is 100 ppm; operating temperature is 500 °C. Response and recovery time were defined as the time needed to reach 90% of the total signal change, respectively.

SnO_2 powders, indicating the advantages of SnO_2 NSs for gas sensing. However, almost a negligible signal was obtained with the presence of 100 ppm ethanol gas for pure SiC NF sensors from 200 to 500 °C (Fig. S5, ESI†), indicating the poor sensing performance of SiC NFs for ethanol gas detection. Obviously, along with the rising operating temperature, the sensitivities ($S = R_a/R_g$) of the three sensors increase initially to the highest value and then drop with a further increase of the temperature. The optimum temperature is found to be 350 °C for the sensors based on pure SnO_2 NSs and SnO_2 NS@SiC NFs. At relatively low temperature (<350 °C), the low sensitivity can be attributed to the insufficient energy to overcome the reaction activation energy barrier.[38] At the temperature higher than 350 °C, the reduction in sensitivity may be due to the difficulty in exothermic gas adsorption.[39] It has been demonstrated that the interaction between gas molecules and SnO_2 surfaces is an exothermic reaction.[40] The accumulation of a large amount of heat energy on the SnO_2 surface leads to the fast desorption of gas molecules before reacting with the oxygen species on the SnO_2 surface at higher temperature,[34] resulting in an obvious drop in sensor response. The higher sensitivity of the SnO_2 NS@SiC NF sensor than that of the pure SnO_2 NS sensor is contributed to the heterojunction effect of SnO_2 and SiC, the specific hierarchical structure and the vertical growth of SnO_2 NSs.

Excitingly, the SnO_2 NS@SiC NF sensor still presents a high sensitivity of 7.2 (*vs.* 3.1 for the pure SnO_2 NS sensor) even at the high temperature of 500 °C, confirming the great potential of SnO_2 NS@SiC NFs for application in high temperature environments. An additional reason may be attributed to the high thermal conductivity of SiC, which can rapidly remove part of heat energy to keep the redox reaction on the SnO_2 surface.

Fig. 7b shows the dynamic sensing responses of the sensors based on pure SnO_2 NSs and SnO_2 NS@SiC NFs toward various ethanol concentrations (10–500 ppm) at the optimized temperature of 350 °C. It can be found that the sensitivities of both the sensors are highly dependent on the ethanol concentration in the measurement range. As the sensitivity–concentration plot shown in Fig. S6 (ESI†), the sensitivities of the two sensors almost increase linearly with the increment of ethanol concentration, particularly at the concentration lower than 100 ppm. The successive response change exhibits the consecutive detection capability of the sensors to target gases even at high temperature. Moreover, the resistance of the sensor goes back to almost the same value when 10 ppm of ethanol was injected into the chamber again. The result suggests the excellent reproducibility of the SnO_2 NS@SiC NF sensor.

Similar orderliness between sensitivity and concentration can also be obtained at the elevated temperature of 500 °C

(Fig. S7, ESI†), implying the outstanding sensing behavior at high temperature. The sensitivities of the SnO_2 NS@SiC NF sensor are from 3.9 to 63.2 for 5–500 ppm ethanol, which is higher than that of the pure SnO_2 NS sensor (1.8–28.4) at the same concentration, further demonstrating the superior sensing performance of SnO_2 NS@SiC NFs. Even when the ethanol concentration is as low as 500 ppb, the sensitivity of the SnO_2 NS@SiC NF sensor can reach 1.2 (Fig. S8, ESI†), indicating the low detect limit of the sensor.

To investigate the reproducibility of the SnO_2 NS@SiC NF sensor, the same sensor was exposed to ethanol with the same concentration for 5 cycles (Fig. 7c). Evidently, consistent sensing responses with excellent recovery characteristics were observed in comparison to the usual significant baseline drift for the SnO_2 sensor,[1] indicating the excellent reproducibility of our sensor. The response and recovery times (τ_{res} and τ_{recov}), which are accordingly defined as the time to achieve 90% of the total resistance change in the case of adsorption (reaching the maximum response) and desorption (back to the original resistance), are also important characteristic parameters for gas sensors. As shown in Fig. 7d, the τ_{res} and τ_{recov} of the SnO_2 NS@SiC NF sensor are respectively found to be 4 and 6 s at 500 °C, which are much faster than those of the SnO_2 NS sensor (7 and 30 s, respectively) and commercial SnO_2 powders (11 s and 29 s, respectively, Fig. S9, ESI†). Even at the temperature of 350 °C, the SnO_2 NS@SiC NF sensor show τ_{res} of 6 s and τ_{recov} of 35 s, corresponding to 1.6 and 5 times faster than those of the pure SnO_2 NS sensor (Fig. S10, ESI†). Very recently, the hierarchical Zn doped SnO_2 nanosheets were reported to present a slow τ_{res} of 14 s toward 100 ppm ethanol at 320 °C.[41] Such rapid response and recovery speeds of our sensor are ascribed to the specific

hierarchical architectures and the vertically ultrathin nanosheet morphology, which can maximize the contact area between the gas molecules and the sensor to facilitate the adsorption and desorption of the ethanol molecular. In the case of pure SnO_2 NSs, it can be seen that the sphere-like SnO_2 NSs obviously aggregate together and some SnO_2 NSs are covered by nanosheets (Fig. S4, ESI†), which results in the low effective reactive area and the resort of the gas.

The advantages of the hierarchical structure to accelerate the adsorption and desorption of target gases were also validated by measuring the response/recovery characteristics of the SnO_2 NS@SiC NF sensor towards various gases (e.g., reducing gases, methanol, isopropanol, acetone, hydrogen and xylene) as illustrated in Fig. 8. It can be seen that all of the τ_{res} values are less than 5 s (for methanol, τ_{res} = 3 s; isopropanol, τ_{res} = 3 s; acetone, τ_{res} = 4 s; hydrogen, τ_{res} = 1 s; xylene, τ_{res} = 5 s), while the τ_{recov} are in the range of 9–15 s (for methanol, τ_{recov} = 9 s; isopropanol, τ_{recov} = 13 s; acetone, τ_{recov} = 7 s; hydrogen, τ_{recov} = 15 s; xylene, τ_{recov} = 10 s). In addition, the response and recovery speeds of our sensor are among the fastest in contrast to the reported SnO_2-based gas sensors recently (Table S1, ESI†), further demonstrating the excellent response/recovery behavior of our SnO_2 NS@SiC NF gas sensor. Fig. 8f shows the sensing selectivity of the SnO_2 NS@SiC NF sensor upon exposure to various gases, including ethanol, methanol, isopropanol, acetone, hydrogen and xylene. Among the investigated gases, the sensor shows the strongest response toward ethanol, which is 1.6 times to hydrogen and 2–4 times to other gases. The result suggests the prepared SnO_2 NS@SiC NF sensor exhibits an ethanol sensing selectivity. The different adsorption abilities and activities of different target gases on the SnO_2 NS@SiC NFs are different at a
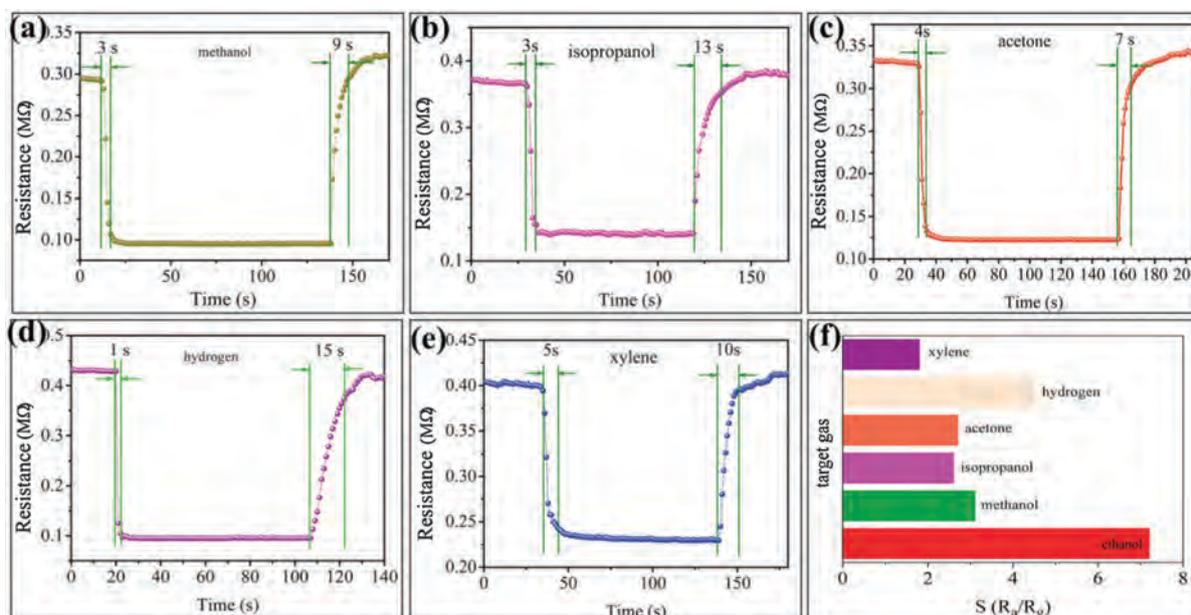

Fig. 8 Ultrafast response/recovery performance of the SnO_2 NS@SiC NF hierarchical composite sensor toward: (a) methanol; (b) isopropanol; (c) acetone; (d) hydrogen and (e) xylene; (f) is the comparison of the sensitivity among various gases, implying the high selectivity of the sensor toward ethanol. The gas concentration is 100 ppm and the operating temperature is 500 °C.
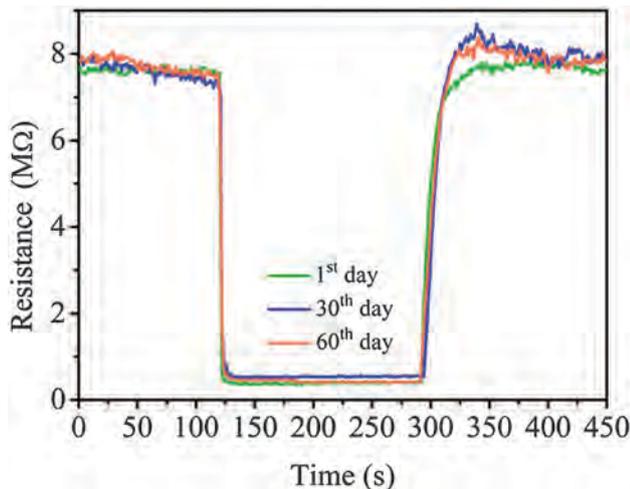
This journal is © The Royal Society of Chemistry 2016

J. Mater. Chem. C, 2016, 4, 295–304 | 301

Fig. 9 The response/recovery behavior of the hierarchical SnO$_2$ NS@SiC NF sensor after 30 and 60 days, implying the superior long-term stability of the sensor.

given temperature, which may result in the superior sensing selectivity of SnO$_2$ NS@SiC NFs.[18]

The sensing performances of the SnO$_2$ NS@SiC NF sensor towards ethanol were measured after 30 and 60 days, respectively, to investigate the long-term stability of the sensor. As shown in Fig. 9, the gas sensor displays a constant response/recovery behavior as well as the sensitivity toward ethanol after 30 and 60 days, demonstrating the superior long-term stability of SnO$_2$ NS@SiC NFs.

Collectively, the SnO$_2$ NS@SiC NF sensor shows high sensitivity, excellent reproducibility, good sensing selectivity, outstanding long-term stability and particularly ultrafast response/recovery speed toward ethanol, even at high temperature. A proposed sensing mechanism is illustrated in Fig. 10. Firstly, the ultrathin SnO$_2$ NSs with a high surface-to-volume ratio were vertically grown on the SiC NFs, supplying a three-dimensional attacking
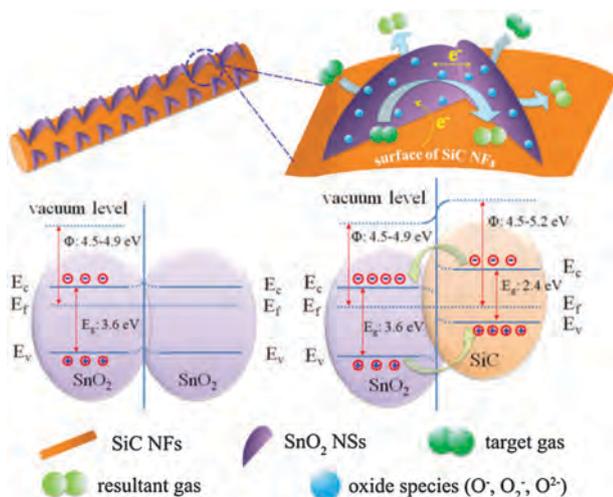

Fig. 10 Proposed sensing mechanism for the high sensitivity and ultrafast response/recovery rate of the SnO$_2$ NS@SiC NFs.

possibility for the target gases. The target gases can react with oxygen species on the SnO$_2$ NSs from the discretional direction. Benefiting from the hierarchical architectures, each of the SnO$_2$ NSs on the SiC NFs contributes to the sensing sites, while the pure SnO$_2$ NSs have a relatively low sensing area because of their aggregation. Secondly, thanks to the *in situ* fabrication process as illustrated in Scheme 1, the SiC NFs and SnO$_2$ NSs are tightly connected to form a heterojunction. And the potential barrier between SnO$_2$ and SiC is very low since the work function of SnO$_2$ (4.5–4.9 eV)[11,42] is just a little smaller than that of SiC (4.5–5.2 eV).[43,44] These two reasons make it easy for the electron transfer from the CB of SiC to the CB of SnO$_2$, and simultaneously the holes on the valence band (VB) of SnO$_2$ can travel to the VB of SiC. At the same time, a built-in potential barrier between SiC NFs and SnO$_2$ NSs is established. The efficient charge separation extends the lifetime of the charge carriers, promoting the charge transfer efficiency of the interface to SnO$_2$.[45] Thirdly, the ultrathin SnO$_2$ NSs are tightly connected together forming a homojunction potential barrier between SnO$_2$ NSs. Blocked by the built-in potential barrier and homojunction potential barrier, the electron transporting in the system is greatly restricted. Thereupon, more oxygen species are absorbed on the surface of SnO$_2$ NSs (in SnO$_2$ NS@SiC NFs) due to the extra electrons on SnO$_2$ NSs, which are provided by the migration of electrons at the heterojunction interface. For reducing target gases (denoted as R, electron donor), more gas molecules can be oxidized by the oxygen species (R + O$^-$ → RO + e$^-$). Thus larger amounts of electrons will be released back to SnO$_2$ NSs, further decreasing the resistance of the SnO$_2$ NS@SiC NF sensor. It has also been demonstrated that the resistance is exponentially proportional to the effective barrier height, $R = R_0 \exp(qV/kT)$, where R and R_0 are accordingly the real and initial resistances of the sensor, and qV is the potential barrier height.[46] Obviously, the reaction between the target gases and the sensor will change the two potentials barriers in the sensor system, further leading to a significant change in the resistance of the sensor. As a consequence, the SnO$_2$ NS@SiC NF sensor shows a higher response than the SnO$_2$ NS sensor.

Although a relatively fast response/recovery speed can be obtained at higher temperature due to the more energy to accelerate the desorption of gases and the reaction between target gases and the sensing materials, that is not the main reason in the case of our SnO$_2$ NS@SiC NF sensor. In fact, the response/recovery speed of the SnO$_2$ NS@SiC NF sensor is much faster than those of the commercial SnO$_2$ powders and the pure SnO$_2$ NS sensor at the same operating temperature. It is reported that 3C-SiC owns high electron mobility due to the enhanced oxygen concentration accumulated at the crystal defects.[47–49] Therefore, the quasi-one-dimensional SiC NF core with high aspect ratios can supply a continuous transport pathway for the fast charge transfer.[27,50] Moreover, the accessible electron transfer between the SnO$_2$ NSs (contacted closely with each other as shown in Fig. 3c) and the heterojunction of SnO$_2$–SiC accelerate the electron transport in the sensor. These lead to the faster response rate of the SnO$_2$ NS@SiC NF sensor. In the case of the desorption process, the resultant gases can

302 | J. Mater. Chem. C, 2016, 4, 295–304

This journal is © The Royal Society of Chemistry 2016

leave the surface of SnO$_2$ NS@SiC NFs almost without any hindrance due to the hierarchical structure of vertical SnO$_2$ NSs on SiC NFs. It has been demonstrated that the hierarchical architectures can provide a method to maximize the interfacial area for effective electron transfer and gas diffusion, thus leading to fast sensing response and recovery of sensors.[51,52] However, the gases are detained by the aggregated SnO$_2$ of the pure SnO$_2$ NS sensor, which results in its slower recovery rate. Taken together, the higher response and the fast response/recovery rate of the SnO$_2$ NS@SiC NF sensor are attributed to the accessible electron transfer at the interface of the SnO$_2$–SiC heterojuction as well as the specific hierarchical architectures of vertical ultrathin SnO$_2$ NS@SiC NFs.

Conclusions

In conclusion, vertically ultrathin SnO$_2$ NSs were *in situ* grown on the quasi-one-dimensional SiC NFs forming a hierarchical architecture *via* a simple hydrothermal method. Compared with commercial SnO$_2$ powders and pure SnO$_2$ NSs, the SnO$_2$ NS@SiC NF hierarchical composite exhibited a superior gas sensing performance including high sensitivity, excellent reproducibility, outstanding sensing selectivity, long-term stability and particularly ultrafast response/recovery rate toward ethanol among the target gases (ethanol, methanol, isopropanol, acetone, hydrogen and xylene), even at high temperature (500 °C). Such a superior sensing performance is attributed to the synergic effect of SnO$_2$–SiC heterojunction, the hierarchical structure as well as the vertical growth of the ultrathin nanosheet morphology. This work may be directional to design high performance gas sensors for application in harsh environments.

Notes and references

1 A. Kaushik, R. Kumar, S. K. Arya, M. Nair, B. D. Malhotra and S. Bhansali, *Chem. Rev.*, 2015, **115**, 4571–4606.

2 M. W. G. Hoffmann, L. Mayrhofer, O. Casals, L. Caccamo, F. Hernandez-Ramirez, G. Lilienkamp, W. Daum, M. Moseler, A. Waag, H. Shen and J. D. Prades, *Adv. Mater.*, 2014, **26**, 8017–8022.

3 S. M. Majhi, P. Rai and Y. T. Yu, *ACS Appl. Mater. Interfaces*, 2015, **7**, 9462–9468.

4 S. Singkammo, A. Wisitsoraat, C. Sriprachuabwong, A. Tuantranont, S. Phanichphant and C. Liewhiran, *ACS Appl. Mater. Interfaces*, 2015, **7**, 3077–3092.

5 A. Das, V. Bonu, A. K. Prasad, D. Panda, S. Dhara and A. K. Tyagi, *J. Mater. Chem. C*, 2014, **2**, 164–171.

6 J. H. Lee, A. Katoch, S. W. Choi, J. H. Kim, H. W. Kim and S. S. Kim, *ACS Appl. Mater. Interfaces*, 2015, **7**, 3101–3109.

7 Z. Zhang, X. Zou, L. Xu, L. Liao, W. Liu, J. Ho, X. Xiao, C. Jiang and J. Li, *Nanoscale*, 2015, **7**, 10078–10084.

8 G. Lu, L. E. Ocola and J. Chen, *Adv. Mater.*, 2009, **21**, 2487–2491.

9 S. Xu, Y. Yang, H. Y. Wu, C. Jiang, L. Q. Jing and K. Y. Shi, *J. Inorg. Mater.*, 2013, **28**, 584–588.

10 S. H. Jeong, S. Kim, J. Cha, M. S. Son, S. H. Park, H. Y. Kim, M. H. Cho, M. H. Whangbo, K. H. Yoo and S. J. Kim, *Nano Lett.*, 2013, **13**, 5938–5943.

11 L. Xu, R. Xing, J. Song and H. Song, *J. Mater. Chem. C*, 2013, **1**, 2174–2182.

12 S. Cui, Z. Wen, X. Huang, J. Chang and J. Chen, *Small*, 2015, **11**, 2305–2313.

13 H. Wang, K. Dou, W. Y. Teoh, Y. Zhan, T. F. Hung, F. Zhang, J. Xu, R. Zhang and A. L. Rogach, *Adv. Funct. Mater.*, 2013, **23**, 4847–4853.

14 X. Chen, Z. Guo, W. H. Xu, H. B. Yao, M. Q. Li, J. H. Liu, X. J. Huang and S. H. Yu, *Adv. Funct. Mater.*, 2011, **21**, 2049–2056.

15 H. R. Kim, A. H. I. D. Kim, N. Barsan, U. Weimar and J. H. Lee, *Adv. Funct. Mater.*, 2011, **21**, 4456–4463.

16 J. S. Lee, O. S. Kwon, S. J. Park, E. Y. Park, S. A. You, H. Yoon and J. Jang, *ACS Nano*, 2011, **5**, 7992–8001.

17 J. Zhang, S. Wang, M. Xu, Y. Wang, H. Xia, S. Zhang, X. Guo and S. Wu, *J. Phys. Chem. C*, 2009, **113**, 1662–1665.

18 L. Li, S. He, M. Liu, C. Zhang and W. Chen, *Anal. Chem.*, 2015, **87**, 1638–1645.

19 H. Liu, M. Li, O. Voznyy, L. Hu, Q. Fu, D. Zhou, Z. Xia, E. H. Sargent and J. Tang, *Adv. Mater.*, 2014, **26**, 2718–2724.

20 Y. Liu, J. Parisi, X. Sun and Y. Lei, *J. Mater. Chem. A*, 2014, **2**, 9919–9943.

21 M. T. Soo, K. Y. Cheong and A. F. M. Noor, *Sens. Actuators, B*, 2010, **151**, 39–55.

22 P. Tsiakarasa and A. Demin, *J. Power Sources*, 2001, **102**, 210–217.

23 S. D. Nobrega, M. V. Galesco, K. Giron, D. Z. de Florio, M. C. Steil, S. Georges and F. C. Fonseca, *J. Power Sources*, 2012, **213**, 156–159.

24 L. Li, M. Liu, S. He and W. Chen, *Anal. Chem.*, 2014, **86**, 7996–8002.

25 B. Wang, Y. Wang, Y. Lei, N. Wu, Y. Gou, C. Han and D. Fang, *J. Mater. Chem. A*, 2014, **2**, 20873–20881.

26 J. Chen, J. Zhang, M. Wang and Y. Li, *Sens. Actuators, B*, 2014, **201**, 402–406.

27 M. Kim, I. Oh and J. Kim, *J. Power Sources*, 2015, **282**, 277–285.

This journal is © The Royal Society of Chemistry 2016

J. Mater. Chem. C, 2016, **4**, 295–304 | 303

28 A. Karakuscu, A. Ponzoni, E. Comini, G. Sberveglieri and C. Vakifahmetoglu, *Int. J. Appl. Ceram. Technol.*, 2014, **11**, 851–857.

29 S. Ding, J. S. Chen and X. W. (David). Lou, *Adv. Funct. Mater.*, 2011, **21**, 4120–4125.

30 S. W. Choi, A. Katoch, G. J. Sun, P. Wu and S. S. Kim, *J. Mater. Chem. C*, 2013, **1**, 2834–2841.

31 Y. Bing, Y. Zeng, C. Liu, L. Qiao, B. Zou and W. Zheng, *Nanoscale*, 2015, **7**, 3276–3284.

32 C. Wang, G. Du, K. Ståhl, H. Huang, Y. Zhong and J. Z. Jiang, *J. Phys. Chem. C*, 2012, **116**, 4000–4011.

33 W. Li, S. Ma, Y. Li, G. Yang, Y. Mao, J. Luo, D. Gengzang, X. Xu and S. Yan, *Sens. Actuators, B*, 2015, **211**, 392–402.

34 C. Dong, X. Liu, X. Xiao, G. Chen, Y. Wang and I. Djerdj, *J. Mater. Chem. A*, 2014, **2**, 20089–20095.

35 W. Ke, G. Fang, Q. Liu, L. Xiong, P. Qin, H. Tao, J. Wang, H. Lei, B. Li, J. Wan, G. Yang and Y. Yan, *J. Am. Chem. Soc.*, 2015, **137**, 6730–6733.

36 Y. Wang, B. Wang, Y. Lei, N. Wu, C. Han, Y. Gou and D. Fang, *Appl. Surf. Sci.*, 2015, **335**, 208–212.

37 K. S. W. Sing, D. H. Everett, R. A. W. Haul, L. Moscou, R. A. Pierotti, J. Rouquerol and T. Siemieniewska, *Pure Appl. Chem.*, 1985, **57**, 603–619.

38 B. Mondal, B. Basumatari, J. Das, C. Roychaudhury, H. Saha and N. Mukherjee, *Sens. Actuators, B*, 2014, **194**, 389–396.

39 Y. Wang, Y. Wang, J. Cao, F. Kong, H. Xia, J. Zhang, B. Zhu, S. Wang and S. Wu, *Sens. Actuators, B*, 2008, **131**, 183–189.

40 Y. Chen, X. Wang, C. Shi, L. Li, H. Qin and J. Hu, *Sens. Actuators, B*, 2015, **220**, 279–287.

41 Q. Zhao, D. Ju, X. Deng, J. Huang, B. Cao and X. Xu, *Sci. Rep.*, 2015, **5**, 7874.

42 M. Punginsang, A. Wisitsoraat, A. Tuantranont, S. Phanichphant and C. Liewhiran, *Sens. Actuators, B*, 2015, **210**, 589–601.

43 X. Zhang, Y. Chen, W. Liu, W. Xue, J. Li and Z. Xie, *J. Mater. Chem. C*, 2013, **1**, 6479–6486.

44 Y. Yang, G. Meng, X. Liu, L. Zhang, Z. Hu, C. He and Y. Hu, *J. Phys. Chem. C*, 2008, **112**, 20126–20130.

45 G. Lu, J. Xu, J. Sun, Y. Yu, Y. Zhang and F. Liu, *Sens. Actuators, B*, 2012, **162**, 82–88.

46 J. Liu, S. Gong, Q. Fu, Y. Wang, L. Quan and Z. Deng, *Sens. Actuators, B*, 2010, **150**, 330–338.

47 N. Yang, H. Zhuang, R. Hoffmann, W. Smirnov, J. Hees, X. Jiang and C. E. Nebel, *Anal. Chem.*, 2011, **83**, 5827–5830.

48 K. Rogdakis, M. Bescond, E. Bano and K. Zekentes, *Nanotechnology*, 2007, **18**, 475715.

49 M. Kim, I. Oh and J. Kim, *J. Mater. Chem. A*, 2015, **3**, 3944–3951.

50 C. Han, Y. Wang, Y. Lei, B. Wang, N. Wu, Q. Shi and Q. Li, *Nano Res.*, 2015, **8**, 1199–1209.

51 D. R. Miller, S. A. Akbar and P. A. Morris, *Sens. Actuators, B*, 2014, **204**, 250–272.

52 S. Park, H. Ko, S. Kim and C. Lee, *ACS Appl. Mater. Interfaces*, 2014, **6**, 9595–9600.